# Kagome quantum anomalous Hall effect with high Chern number and large band gap

Zhen Zhang,[1] Jing-Yang You,[2] Xing-Yu Ma,[1] Bo Gu,[2,3,*] and Gang Su[2,3,1,†]

[1]*School of Physical Sciences, University of Chinese Academy of Sciences, Beijng 100049, China*

[2]*Kavli Institute for Theoretical Sciences, and CAS Center for Excellence in Topological Quantum Computation, University of Chinese Academy of Sciences, Beijng 100190, China*

[3]*Physical Science Laboratory, Huairou National Comprehensive Science Center, Beijing 101400, China*

(Received 14 October 2020; accepted 15 December 2020; published 7 January 2021)

Due to the potential applications in low-power-consumption spintronic devices, the quantum anomalous Hall effect (QAHE) has attracted tremendous attention in past decades. However, up to now, the QAHE was only observed experimentally in topological insulators with Chern numbers $C = 1$ and 2 at very low temperatures. Here, we propose three two-dimensional stable kagome ferromagnets $Co_3Pb_3S_2$, $Co_3Pb_3Se_2$, and $Co_3Sn_3Se_2$ that can realize the QAHE with high Chern number of $|C| = 3$. Monolayers $Co_3Pb_3S_2$, $Co_3Pb_3Se_2$, and $Co_3Sn_3Se_2$ possess the large band gap of 70, 77, and 63 meV with Curie temperature $T_C$ of 51, 42, and 46 K, respectively. By constructing a heterostructure $Co_3Sn_3Se_2/MoS_2$, its $T_C$ is enhanced to 60 K and the band gap remains at about 60 meV due to the tensile strain of 2% at the interface. For the bilayer compound $Co_6Sn_5Se_4$, it becomes a half metal, with a relatively flat plateau in its anomalous Hall conductivity corresponding to $|C| = 3$ near the Fermi level. Our results provide topological nontrivial systems of kagome ferromagnetic monolayers and heterostructures possessing the QAHE with high Chern number $|C| = 3$ and large band gaps.

DOI: 10.1103/PhysRevB.103.014410

## I. INTRODUCTION

The quantum anomalous Hall effect (QAHE) was predicted by Haldane in 1988 using a honeycomb lattice model [1]. The QAHE is characterized by the nonzero Chern numbers with the quantized Hall conductance. Owing to the existence of dissipationless chiral edge states, QAHE can be used to design low-power-consumption spintronic devices. Up to now, much effort has been made to search for QAHE materials with large band gap and high Curie temperature ($T_C$), including adsorbing diluted $3d$, $4d$, and $5d$ transition atoms on graphene [2–5]; using surface functionalization on the buckled honeycomb lattice silicene, germanene, and stanlene [6,7]; constructing a heterostructure by depositing atomic layers of elements on a ferromagnetic insulator [8–13]; and applying pure ferromagnetic semiconductor compounds $MX_3$ without external fields or additional doping [14–17]. Despite a lot of theoretical predictions, the observation of the QAHE in experiment is rare. The first observed QAHE with quantized Hall conductance $e^2/h$ was in Cr-doped $(Bi, Sb)_2Te_3$ thin films at a very low temperature of 30 mK [18]. Later, the QAHE in V-doped and Cr-and-V co-doped $(Bi, Sb)_2Te_3$ thin film was observed at about 25 and 300 mK, respectively [19,20]. Recently, the quantized anomalous Hall conductance (AHC) plateau $\sigma_{xy} = e^2/h$ was observed in $MnBi_2Te_4$ thin flakes [21,22]; moreover, a high-Chern-number QAHE with $\sigma_{xy} = 2e^2/h$ was also obtained in a 10-layer $MnBi_2Te_4$ device at about 13 K [23]. However, there have been sparse theoretical reports of the QAHE with higher Chern number such as $C = 3$ [24–27].

Inspired by the Haldane model, in the past decades, most of the QAHE were predicted based on a honeycomb lattice. Nevertheless, a kagome lattice with out-of-plane magnetization is also an important platform for investigating the QAHE [28–32]. In particular, a layered magnetic kagome lattice $Co_3Sn_2S_2$ was recently reported to be a Weyl semimetal with a large intrinsic AHC [33]. Because of the successful synthesis of the bulk $Co_3Sn_2S_2$, monolayer $Co_3Sn_3S_2$ was studied theoretically and was found to be a Chern insulator with $C = 3$ [34].

In this work, inspired by recent studies of $Co_3Sn_3S_2$, we systematically investigate monolayers $Co_3X_3Y_2$ ($X$ = C,Si,Ge,Sn,Pb; $Y$ = O,S,Se,Te,Po) based on the first-principles calculations. Our results show that monolayers $Co_3Pb_3S_2$, $Co_3Pb_3Se_2$, and $Co_3Sn_3Se_2$ are stable. Among them, the bulk form of $Co_3Sn_3Se_2$ has been studied and found to be a magnetic Weyl semimetal [35,36]. According to the results of anomalous Hall conductivity $\sigma_{xy}$ and Chiral edge states, a high Chern number $|C| = 3$ was obtained in these three compounds. Furthermore, we find that the band gap and $T_C$ are all sensitive to the applied strain. For the $Co_3Sn_3Se_2$ monolayer, its band gap can be decreased to zero with compressive strain of $-3\%$, and its $T_C$ can be increased to 65 K with tensile strain of 4%. $T_C = 60$ K and tensile strain of 2% can be obtained by constructing a heterostructure $Co_3Sn_3Se_2/MoS_2$. We have also explored the topological properties of bilayer $Co_3Sn_3Se_2$ and found a Weyl node on the $\Gamma \rightarrow M$ path near the Fermi level. Although there is no global gap, we find a relatively flat plateau in AHC corresponding to $|C| = 3$ near the Fermi level.

*gubo@ucas.ac.cn
†gsu@ucas.ac.cn

 

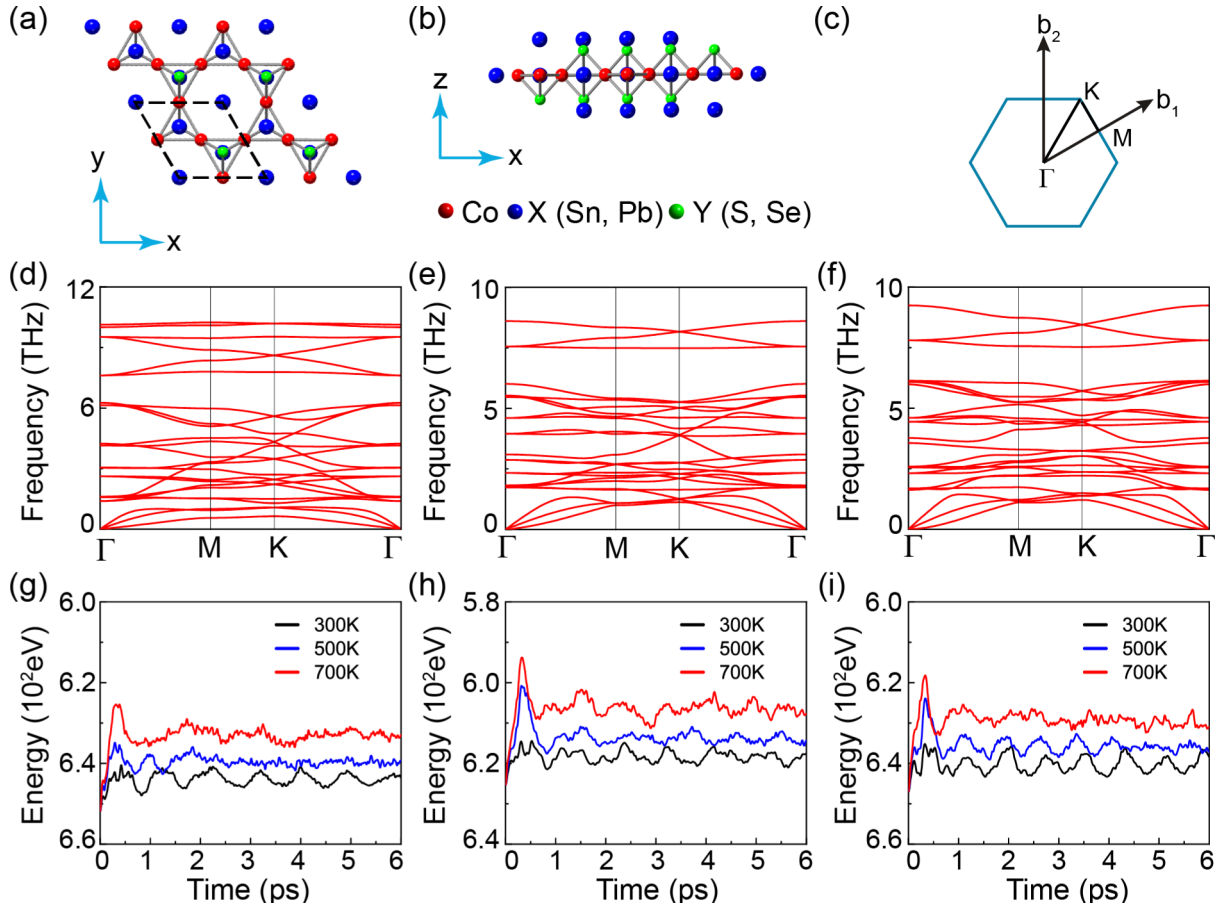


FIG. 1. (a) Top and (b) side views of monolayer $Co_3X_3Y_2$. (c) First Brillouin zone. Phonon spectra of (d) $Co_3Pb_3S_2$, (e) $Co_3Pb_3Se_2$, and (f) $Co_3Sn_3Se_2$ monolayers. Molecular dynamics simulations for (g) $Co_3Pb_3S_2$, (h) $Co_3Pb_3Se_2$, and (i) $Co_3Sn_3Se_2$ at different temperatures for 6 ps with a time step of 3 fs.

## II. COMPUTATIONAL METHODS

In our studies, the first-principles calculations were performed using the projector augmented wave (PAW) method [37] based on the density functional theory (DFT) as implemented in the Vienna *ab initio* simulation package (VASP) [38,39]. The electron exchange-correlation functional is described by the generalized gradient approximation (GGA) in the form proposed by Perdew, Burke, and Ernzerhof (PBE) [40]. A 20 Å vacuum space is built to avoid the interlayer interactions. Lattice constants and atomic positions are fully optimized with the conjugate gradient (CG) scheme until the maximum force acting on all atoms is less than $1 \times 10^{-3}$ eV/Å and the total energy is converged to $10^{-7}$ eV. The $9 \times 9 \times 1$ and $15 \times 15 \times 1$ $K$ meshes generated by a Γ-centered Monkhorst-Pack grid [41] are used for structure optimization and self-consistent calculations. The plane-wave cutoff energy is set to be 500 eV. The phonon frequency calculations have been carried out using the finite displacement approach as implemented in the PHONOPY code [42] with a $4 \times 4 \times 1$ supercell. The thermal stability is examined by performing molecular dynamics (MD) simulations in the canonical ($NVT$) ensemble in a $4 \times 4 \times 1$ supercell at different temperatures with a Nosé thermostat. In the calculation of the $Co_3Sn_3Se_2/MoS_2$ heterostructure, the zero-damping DFT-D3 method is adopted to take interlayer van der Waals forces into account. Surface states are investigated by an effective tight-binding Hamiltonian constructed from the maximally localized Wannier functions [43,44]. And the iterative Green function method [45] is used with the package WANNIERTOOLS [46].

## III. DFT RESULTS OF MONOLAYERS $Co_3Pb_3S_2$, $Co_3Pb_3Se_2$, AND $Co_3Sn_3Se_2$

### A. Crystal structure and stability

The crystal structure of $Co_3X_3Y_2$ ($X$ = Sn,Pb; $Y$ = S,Se) with the space group $P3m1$ (No. 164) is depicted in Figs. 1(a) and 1(b). Co atoms form a two-dimensional (2D) kagome lattice with one $X$ atom sandwiched by $X$ and $Y$ atoms in the center. Each primitive cell contains one formula unit. The calculated lattice constants for $Co_3Pb_3S_2$, $Co_3Pb_3Se_2$, and $Co_3Sn_3Se_2$ are 5.38, 5.44, and 5.32 Å, respectively. After checking the dynamical stabilities of all compounds $Co_3X_3Y_2$ ($X$ = C,Si,Ge,Sn,Pb; $Y$ = O,S,Se,Te,Po) by calculating their phonon spectra, we found that only $Co_3Pb_3S_2$, $Co_3Pb_3Se_2$, and $Co_3Sn_3Se_2$ monolayers are dynamically stable because there are no imaginary phonon modes in the whole Brillouin zone, as shown in Figs. 1(d)–1(f). The stabilities of these compounds are also checked by the formation energy, which is defined as $E_f = E_{Co_3X_3Y_2} - 3E_{Co} - 3E_X - 2E_Y$,

TABLE I. The calculated energy difference ($\Delta E$) between the ferromagnetic and antiferromagnetic configurations per primitive cell, magnetic moment ($M$), magnetic anisotropy energy (MAE), band gap, nearest-neighbor exchange integral ($J|S|^2$) where $S$ is the spin at the Co atom, single-ion anisotropy ($D|S|^2$), Curie temperature ($T_C$), and the maximum Kerr angle ($\theta_{\text{Kerr}}$) for $Co_3Pb_3S_2$, $Co_3Pb_3Se_2$, and $Co_3Sn_3Se_2$ monolayers.

| | $Co_3Pb_3S_2$ | $Co_3Pb_3Se_2$ | $Co_3Sn_3Se_2$ |
|---|---|---|---|
| $\Delta E$ (meV) | −60.5 | −44.8 | −51.5 |
| $M$ ($\mu_B$) | 0.42 | 0.43 | 0.39 |
| MAE (meV/Co) | 0.42 | 0.73 | 0.65 |
| Gap (meV) | 70 | 77 | 63 |
| $J\|S\|^2$ (meV) | 6.73 | 4.98 | 5.73 |
| $D\|S\|^2$ (meV) | 0.42 | 0.73 | 0.65 |
| $T_c$ (K) | 51 | 42 | 46 |
| $\theta_{\text{Kerr}}$ (deg) | 2.25 | 2.83 | 1.28 |

where $E_{Co_3X_3Y_2}$ is the energy of the $Co_3X_3Y_2$ monolayer, $E_{Co}$, $E_X$, and $E_Y$ are the energies of common elementary substances corresponding to Co, $X$, and $Y$ elements, i.e., hcp (hexagonal closest packed) Co, fcc (face-centered cubic) Pb or diamond cubic Sn, and monoclinic S or Se, respectively. The obtained negative values −0.75, −0.28, and −0.80 eV per primitive cell indicate exothermic reactions for $Co_3Pb_3S_2$, $Co_3Pb_3Se_2$, and $Co_3Sn_3Se_2$. The ternary convex hull diagrams are used to further check the thermodynamic stabilities, as studied in the Supplemental Material [47]. Based on the elementary and binary materials in the Materials Project [48], which have been synthesized experimentally, we have studied serval different routes to synthesize $Co_3Sn_3Se_2$, $Co_3Pb_3S_2$, and $Co_3Pb_3Se_2$. The results show that all three compounds $Co_3Sn_3Se_2$, $Co_3Pb_3S_2$, and $Co_3Pb_3Se_2$ are in metastable states. Since some metastable materials have been synthesized in experiments, such as the binary compounds $CoSn_2$ [49], it is expected that the materials proposed here can also be experimentally realized in the future. Their thermal stabilities are then confirmed by the molecular dynamics simulations performed in a $4 \times 4 \times 1$ supercell at 300, 500, and 700 K, respectively. As shown in Figs. 1(g)–1(i), the small fluctuation of total energy indicates their thermal stabilities.

### B. Magnetic and electronic properties

The ferromagnetic (FM) and four antiferromagnetic (AFM) spin configurations, as shown in Fig. S4 in the Supplemental Material [47], are studied for $Co_3Pb_3S_2$, $Co_3Pb_3Se_2$, and $Co_3Sn_3Se_2$ monolayers. Among these spin configurations, the FM configuration possesses the lowest energy, indicating the FM ground states of these monolayers. For spin configurations AFM2, AFM3, and AFM4, the zero magnetic moments of some Co atoms are obtained after optimization calculations, and we neglect these unphysical results. So, here we consider the spin configurations FM and AFM1 (120° in-plane spin polarization) [50] to calculate the exchange couplings. The energy difference between these two configurations, which is defined as $\Delta E = E_{\text{FM}} - E_{\text{AFM}}$, is listed in Table I. For the FM ground state, the magnetic anisotropy energy (MAE), which is defined as the energy difference

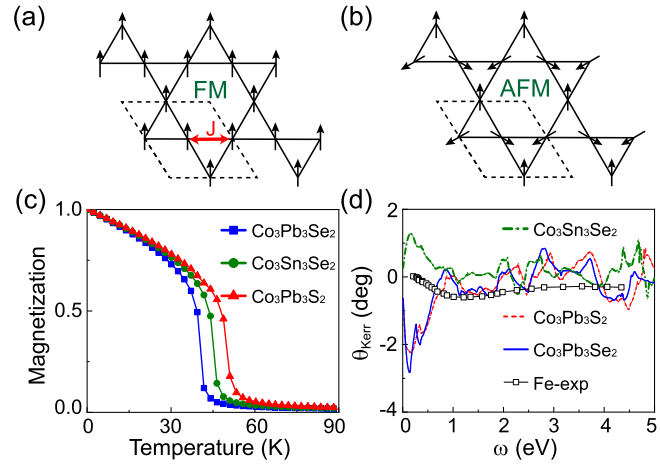


FIG. 2. (a) Ferromagnetic (FM) and (b) antiferromagnetic (AFM) spin configurations for Co atoms in the kagome lattice. For $Co_3Pb_3S_2$, $Co_3Pb_3Se_2$, and $Co_3Sn_3Se_2$ monolayers, the (c) temperature-dependent normalized magnetic moment and (d) Kerr angle as a function of photon energy.

between the total energies corresponding to the in-plane and out-of-plane FM configurations for these three compounds, is calculated as listed in Table I. One may see that all these compounds prefer an out-of-plane magnetization.

The magnetism of these compounds can be described by the following Heisenberg-type Hamiltonian:

$$H_0 = -\sum_{\langle i,j \rangle} J \boldsymbol{S_i} \cdot \boldsymbol{S_j} - \sum_{\langle i \rangle} D S_{iz}^2, \tag{1}$$

where $J$ and $D$ are the nearest-neighbor exchange integral and single-ion anisotropy (SIA), respectively. In order to obtain $J|S|^2$ and $D|S|^2$, the energies corresponding to three different magnetic configurations, FM($\boldsymbol{m} \parallel \boldsymbol{x}$), FM($\boldsymbol{m} \parallel \boldsymbol{z}$), and AFM, are expressed as

$$\begin{aligned} E_{FM(\boldsymbol{m}\parallel\boldsymbol{x})} &= -6J|\boldsymbol{S}|^2 + E_0, \\ E_{FM(\boldsymbol{m}\parallel\boldsymbol{z})} &= -6J|\boldsymbol{S}|^2 - 3D|\boldsymbol{S}|^2 + E_0, \\ E_{AFM} &= 3J|\boldsymbol{S}|^2 + E_0, \end{aligned} \tag{2}$$

where $E_0$ is the energy which is independent of the spin configurations. The corresponding $J|S|^2$ and $D|S|^2$ are listed in Table I. The Monte Carlo (MC) simulations on a $80 \times 80 \times 1$ kagome lattice with periodic boundary conditions are carried out with each temperature calculation containing $10^6$ MC steps [51]. The Curie temperatures are estimated to be 51, 42, and 46 K for $Co_3Pb_3S_2$, $Co_3Pb_3Se_2$, and $Co_3Sn_3Se_2$ monolayers, respectively, as shown in Fig. 2(c). The magneto-optical Kerr effect is usually expected in FM materials due to their potential applications in magneto-optical storage devices. For FM materials with magnetization perpendicular to the surface and at least threefold rotational symmetry along $\mathbf{z}$, the Kerr rotation angle can be written as $\theta_{\text{Kerr}} = -\text{Re}\frac{\epsilon_{xy}}{(\epsilon_{xx}-1)\sqrt{\epsilon_{xx}}}$, where $\omega$ is the photon energy, and $\epsilon_{xx}$ and $\epsilon_{xy}$ are the diagonal and off-diagonal terms of the dielectric tensor $\epsilon$ [52–55]. And the dielectric tensor $\epsilon$ has a relationship with optical conductivity tensor $\sigma$ that could be expressed as $\sigma(\omega) = \frac{\omega}{4\pi i}[\epsilon(\omega) - I]$, where $I$ is a unit tensor. The optical conductivity tensor $\sigma$

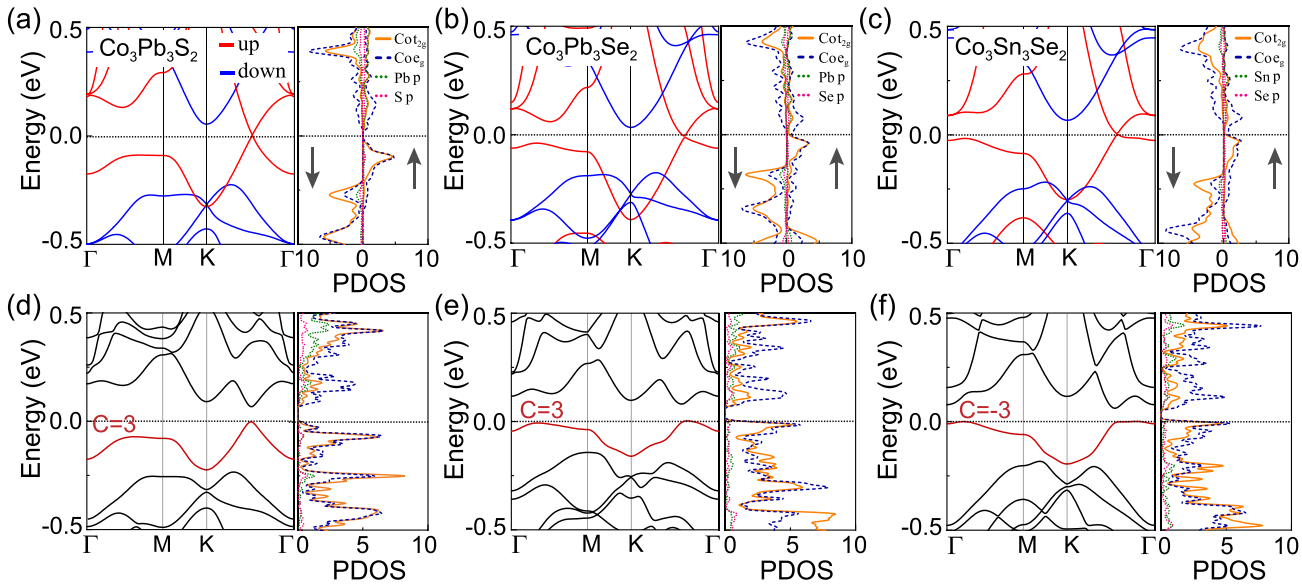


FIG. 3. Electronic band structure and projected density of states for monolayers (a) $Co_3Pb_3S_2$, (b) $Co_3Pb_3Se_2$, and (c) $Co_3Sn_3Se_2$ without spin-orbit coupling (SOC). (d)–(f) The corresponding results with inclusion of SOC, respectively.

and Kerr rotation angle can be obtained using VASP along with WANNIER90. The photon energy dependent Kerr angles are illustrated in Fig. 2(d). The sign of the Kerr angles of $Co_3Pb_3S_2$ and $Co_3Pb_3Se_2$ differs from $Co_3Sn_3Se_2$ in the low photon energy range, due to the opposite sign of $\epsilon_{xy}$. For these three compounds, at the photon energy of about 0.2 eV, the Kerr angles reach the maximum values of about 2.9°, as listed in Table I, which is much larger than the reported 0.8° for Fe bulk and is comparable to the Tc-based ferromagnetic semiconductors [56].

The spin-polarized band structures were calculated as shown in Fig. 3. In the absence of spin-orbit coupling (SOC), they all behave as a Weyl half semimetal [16] with a fully spin-polarized Weyl point on the $K \rightarrow \Gamma$ path near the Fermi level. Because of the symmetries, there should be three pairs of Weyl nodes in the whole Brillouin zone (BZ). The corresponding partial density of states (PDOS) show that the density of states near the Fermi level is mainly attributed to the $t_{2g}$ and $e_g$ orbitals of Co atoms. After including SOC, the band gaps of about 70, 77, and 63 meV are opened for $Co_3Pb_3S_2$, $Co_3Pb_3Se_2$, and $Co_3Sn_3Se_2$, respectively.

### C. Topological properties

In order to investigate their topological properties, maximally localized Wannier functions (MLWFs) implemented in the WANNIER90 package are employed to fit their DFT band structures. Nonzero Chern number $C$ is viewed as a character of the topologically nontrivial band structure and, for each band, the Chern number can be obtained by integrating the Berry curvature over the first Brillouin zone. The calculated Chern number $C$ for the valence band near the Fermi level is marked in Fig. 3. Figures 4(a)–4(c) show the calculated anomalous Hall conductance as a function of the chemical potential, and the quantized charge Hall plateau of $\sigma_{xy} = Ce^2/h$ is obtained when the chemical potential is within the band gap, characterizing the QAHE. Furthermore, the QAHE can also be confirmed by calculating their chiral edge states appearing within the band gap. On the basis of a recursive strategy, we construct the MLWFs using all $d$ orbitals of the Co atoms and calculate their local density of the edge states as shown in Figs. 4(d)–4(f). One can see that the bulk states are connected by three topologically nontrivial edge states. As the number of edge states cutting the Fermi level indicates the value of the Chern number, $|C| = 3$ is further verified. The internal of the Berry curvature in a region around one original Weyl point gives a Chern number of 1/2. There are six Weyl points related by $C_3$ and inversion symmetry that should have the same Chern number of 1/2. Thus we can obtain the Chern number 3.

### D. STRAIN EFFECT AND $Co_3Sn_3Se_2/MoS_2$ HETEROSTRUCTURE

To investigate the effect of strain on $Co_3X_3Y_2$ monolayers, as shown in Fig. 5, we plot the band gap and Curie temperature $T_C$ of the $Co_3Sn_3Se_2$ monolayer as a function of biaxial strain, which is defined as $\varepsilon = (a - a_0)/a_0$, where $a$ and $a_0$ are the strained and equilibrium lattice parameters, respectively. With the increase of compressed strain, the valence-band maximum (VBM) value at Γ point is lifted, while the conduction-band minimum (CBM) value drops at the $K$ point, leading to the gradual closure of the band gap. The VBM at the Γ point and CBM at the $K$ point move in the opposite directions relative to the Fermi level with the tensile strain, and thus the band gap remains at about 60 meV. Meanwhile, the applied tensile strain will enhance the exchange-coupling parameter $J$ and the corresponding Curie temperature from 46 to 65 K. The strain effect on the band gap and $T_c$ for $Co_3Pb_3S_2$ and $Co_3Pb_3Se_2$

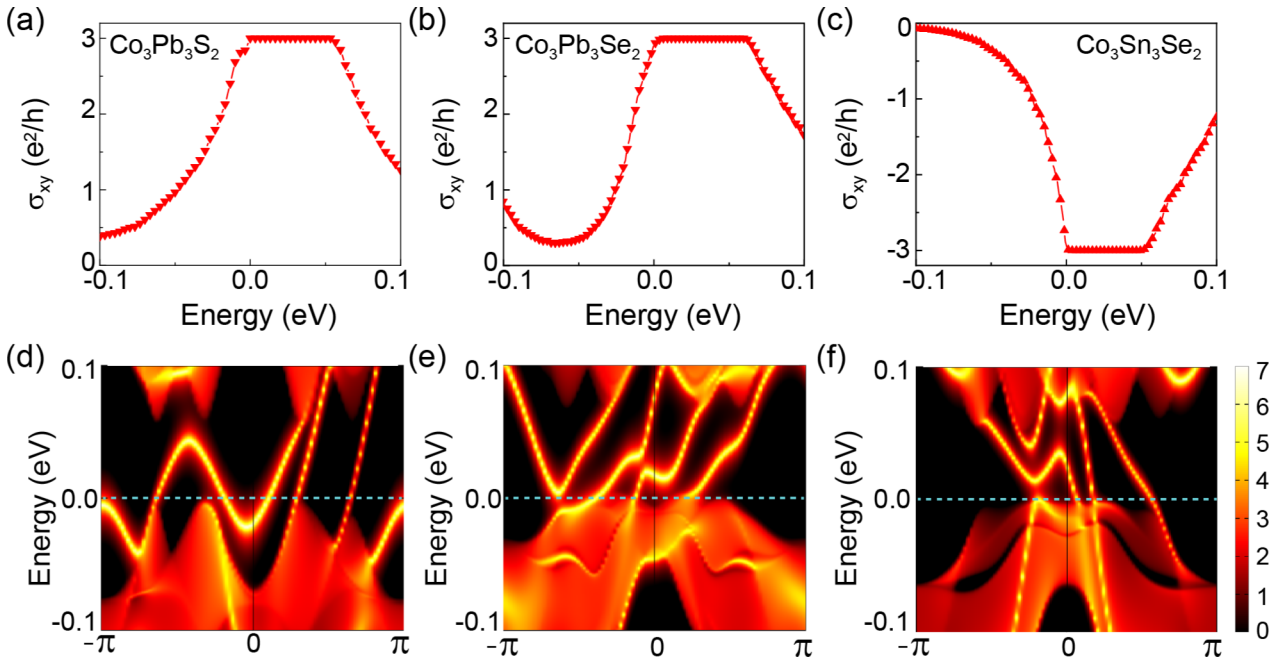


FIG. 4. The anomalous Hall conductance for monolayers (a) $Co_3Pb_3S_2$, (b) $Co_3Pb_3Se_2$, and (c) $Co_3Sn_3Se_2$. (d)–(f) The corresponding chiral edge states projected on the (100) surface, where the bright lines show the chiral edge states, respectively.

has also been studied, as shown in Fig. S6 of the Supplemental Material, where similar behavior is obtained [47].

To investigate the effect of the substrate on the electronic properties of $Co_3X_3Y_2$ monolayers, we construct a heterostructure $Co_3Sn_3Se_2/MoS_2$ as shown in Fig. 6(a). The heterostructure consists of a $1 \times 1$ unit cell of $Co_3Sn_3Se_2$ and a $\sqrt{3} \times \sqrt{3}$ unit cell of $MoS_2$. The lattice mismatch at the interface is only 2%. By the first-principles calculations with the van der Waals (vdW) interaction, the optimized lattice constant and equilibrium interlayer distance $d$ for the heterostructure is about 5.42 Å and 2.76 Å, respectively. The $T_C$ is enhanced up to 60 K, with the band gap remaining at about 60 meV. The calculated AHC and edge states, as shown in Figs. 6(b) and 6(c), indicate that the topological property of $Co_3Sn_3Se_2$ preserves.

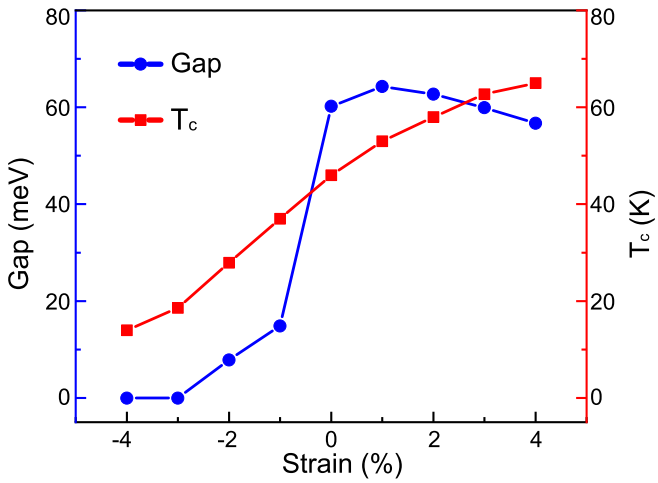


FIG. 5. Band gap and Curie temperature as functions of applied biaxial strain of monolayer $Co_3Sn_3Se_2$.

### E. PROPERTIES of $Co_6Pb_5S_4$, $Co_6Pb_5Se_4$, AND $Co_6Sn_5Se_4$ BILAYERS

To study the layer-dependent topological properties, the stabilities of the bilayer compounds $Co_6Pb_5S_4$, $Co_6Pb_5Se_4$, and $Co_6Sn_5Se_4$ are first confirmed by calculating the phonon spectra, where no imaginary frequency was observed, as shown in Fig. S7 of the Supplemental Material [47]. For $Co_6Sn_5Se_4$, we have noticed that a Weyl node appears at the $\Gamma \rightarrow M$ path near the Fermi level, as illustrated in Fig. 7(b). Taking the SOC into account, a local band gap of about 51 meV at the (original) Weyl point is opened. Although there

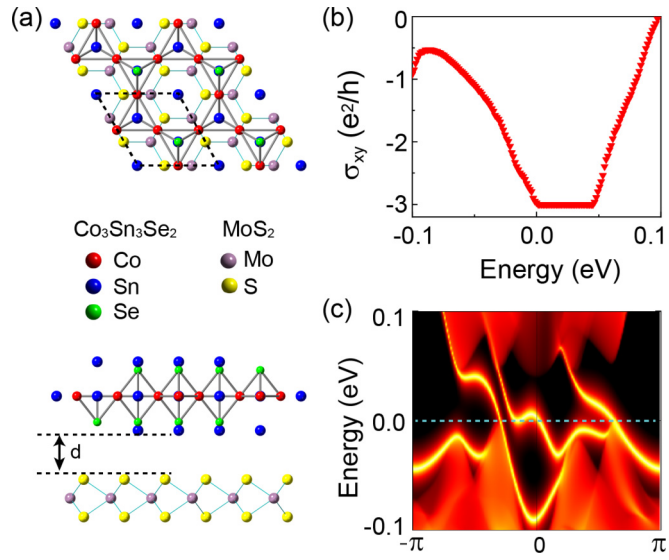


FIG. 6. For the heterostructure $Co_3Sn_3Se_2/MoS_2$, (a) top and side views of crystal structure, (b) anomalous Hall conductance, and (c) chiral edge states.

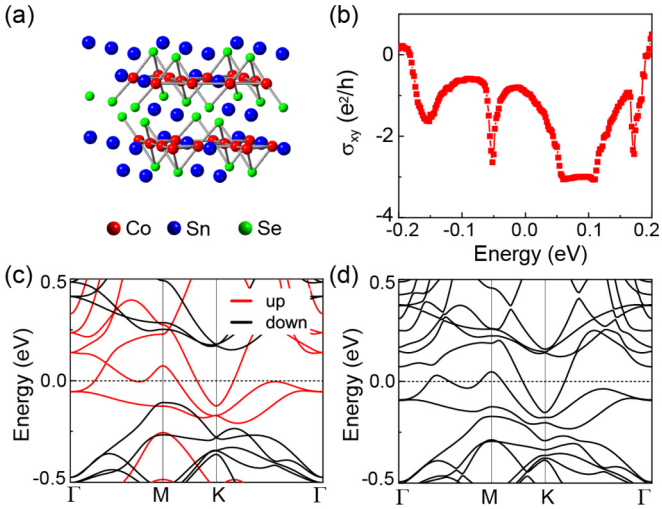


FIG. 7. For bilayer compound $Co_6Sn_5Se_4$, (a) crystal structure, (b) band structure without spin-orbit coupling (SOC), (c) band structure with SOC, and (d) anomalous Hall conductance.

is no global gap, it is interesting to find a relatively flat plateau of AHC corresponding to $|C| = 3$ near the Fermi level.

## IV. CONCLUSION

By using first-principles calculations, we have systematically investigated the two-dimensional kagome ferromagnets $Co_3Pb_3S_2$, $Co_3Pb_3Se_2$, and $Co_3Sn_3Se_2$ monolayers, which can realize the high-Chern-number ($|C| = 3$) QAHE with a large band gap. For the $Co_3Pb_3S_2$, $Co_3Pb_3Se_2$, and $Co_3Sn_3Se_2$ monolayers, the band gap of 70, 77, and 63 meV and $T_C$ of 51, 42, and 46 K are obtained, respectively. By constructing a heterostructure $Co_3Sn_3Se_2/MoS_2$, the $T_C$ can be enhanced to 60 K and the band gap remains at about 60 meV due to the tensile strain of 2% at the interface. For the bilayer compound $Co_6Sn_5Se_4$, it becomes a half metal with a relatively flat plateau in its anomalous Hall conductivity corresponding to $|C| = 3$ near the Fermi level. Our results provide topologically nontrivial systems of kagome ferromagnetic monolayers and heterostructures with high $|C| = 3$ and large band gap QAHE, which are helpful to deepen our understanding of the topological states in ferromagnets with kagome lattices.

## ACKNOWLEDGMENTS

This work is supported in part by the National Key R&D Program of China (Grant No. 2018YFA0305800), the Strategic Priority Research Program of the Chinese Academy of Sciences (Grant No. XDB28000000), the National Natural Science Foundation of China (Grant No. 11834014), and the Beijing Municipal Science and Technology Commission (Grant No. Z191100007219013). B.G. is also supported by the National Natural Science Foundation of China (Grants No. Y81Z01A1A9 and No. 12074378), the Chinese Academy of Sciences (Grants No. Y929013EA2 and No. E0EG4301X2), the University of Chinese Academy of Sciences (Grant No. 110200M208), the Strategic Priority Research Program of Chinese Academy of Sciences (Grant No. XDB33000000), and the Beijing Natural Science Foundation (Grant No. Z190011).

[1] F. D. M. Haldane, Model for a Quantum Hall Effect without Landau Levels: Condensed-Matter Realization of the "Parity Anomaly", Phys. Rev. Lett. **61**, 2015 (1988).

[2] J. Ding, Z. Qiao, W. Feng, Y. Yao, and Q. Niu, Engineering quantum anomalous valley Hall states in graphene via metal-atom adsorption: An *ab initio* study, Phys. Rev. B **84**, 195444 (2011).

[3] C. M. Acosta, M. P. Lima, R. H. Miwa, A. J. R. da Silva, and A. Fazzio, Topological phases in triangular lattices of Ru adsorbed on graphene: *Ab initio* calculations, Phys. Rev. B **89**, 155438 (2014).

[4] H. Zhang, C. Lazo, S. Blügel, S. Heinze, and Y. Mokrousov, Electrically Tunable Quantum Anomalous Hall Effect in Graphene Decorated by 5d Transition-Metal Adatoms, Phys. Rev. Lett. **108**, 056802 (2012).

[5] J. Hu, Z. Zhu, and R. Wu, Chern half metals: A new class of topological materials to realize the quantum anomalous Hall effect, Nano Lett. **15**, 2074 (2015).

[6] S.-M. Huang, S.-T. Lee, and C.-Y. Mou, Ferromagnetism and quantum anomalous Hall effect in one-side-saturated buckled honeycomb lattices, Phys. Rev. B **89**, 195444 (2014).

[7] S.-C. Wu, G. Shan, and B. Yan, Prediction of Near-Room-Temperature Quantum Anomalous Hall Effect on Honeycomb Materials, Phys. Rev. Lett. **113**, 256401 (2014).

[8] K. F. Garrity and D. Vanderbilt, Chern Insulators from Heavy Atoms on Magnetic Substrates, Phys. Rev. Lett. **110**, 116802 (2013).

[9] Z. Qiao, W. Ren, H. Chen, L. Bellaiche, Z. Zhang, A.H. MacDonald, and Q. Niu, Quantum Anomalous Hall Effect in Graphene Proximity Coupled to an Antiferromagnetic Insulator, Phys. Rev. Lett. **112**, 116404 (2014).

[10] Z. Wang, C. Tang, R. Sachs, Y. Barlas, and J. Shi, Proximity-Induced Ferromagnetism in Graphene Revealed by the Anomalous Hall Effect, Phys. Rev. Lett. **114**, 016603 (2015).

[11] J. Zhang, B. Zhao, Y. Yao, and Z. Yang, Robust quantum anomalous Hall effect in graphene-based van der Waals heterostructures, Phys. Rev. B **92**, 165418 (2015).

[12] J. Zhang, B. Zhao, T. Zhou, Y. Xue, C. Ma, and Z. Yang, Strong magnetization and Chern insulators in compressed graphene/$CrI_3$ van der Waals heterostructures, Phys. Rev. B **97**, 085401 (2018).

[13] R. Zou, F. Zhan, B. Zheng, X. Wu, J. Fan, and R. Wang, Intrinsic quantum anomalous Hall phase induced by proximity in the van der Waals heterostructure germanene/$Cr_2Ge_2Te_6$, Phys. Rev. B **101**, 161108(R) (2020).

[14] X.-L. Sheng and B. K. Nikolić, Monolayer of the 5d transition metal trichloride $OsCl_3$ : A playground for two-dimensional magnetism, room-temperature quantum anomalous Hall effect,

and topological phase transitions, Phys. Rev. B **95**, 201402(R) (2017).

[15] Y. Ping Wang, S. Shi Li, C. Wen Zhang, S. Feng Zhang, W. Xiao Ji, P. Li, and P. Ji Wang, High-temperature Dirac half-metal $PdCl_3$: A promising candidate for realizing quantum anomalous Hall effect, J. Mater. Chem. C **6**, 10284 (2018).

[16] J.-Y. You, C. Chen, Z. Zhang, X.-L. Sheng, S. A. Yang, and G. Su, Two-dimensional Weyl half-semimetal and tunable quantum anomalous Hall effect, Phys. Rev. B **100**, 064408 (2019).

[17] J.-Y. You, Z. Zhang, B. Gu, and G. Su, Two-dimensional room-temperature ferromagnetic semiconductors with quantum anomalous Hall effect, Phys. Rev. Appl. **12**, 024063 (2019).

[18] C.-Z. Chang, J. Zhang, X. Feng, J. Shen, Z. Zhang, M. Guo, K. Li, Y. Ou, P. Wei, L.-L. Wang, Z.-Q. Ji, Y. Feng, S. Ji, X. Chen, J. Jia, X. Dai, Z. Fang, S.-C. Zhang, K. He, Y. Wang *et al.*, Experimental observation of the quantum anomalous Hall effect in a magnetic topological insulator, Science **340**, 167 (2013).

[19] C.-Z. Chang, W. Zhao, D. Y. Kim, H. Zhang, B. A. Assaf, D. Heiman, S.-C. Zhang, C. Liu, M. H. W. Chan, and J. S. Moodera, High-precision realization of robust quantum anomalous Hall state in a hard ferromagnetic topological insulator, Nat. Mater. **14**, 473 (2015).

[20] Y. Ou, C. Liu, G. Jiang, Y. Feng, D. Zhao, W. Wu, X.-X. Wang, W. Li, C. Song, L.-L. Wang, W. Wang, W. Wu, Y. Wang, K. He, X.-C. Ma, and Q.-K. Xue, Enhancing the quantum anomalous Hall effect by magnetic codoping in a topological insulator, Adv. Mater. **30**, 1703062 (2017).

[21] Y. Deng, Y. Yu, M. Z. Shi, Z. Guo, Z. Xu, J. Wang, X. H. Chen, and Y. Zhang, Quantum anomalous Hall effect in intrinsic magnetic topological insulator $MnBi_2Te_4$, Science **367**, 895 (2020).

[22] C. Liu, Y. Wang, H. Li, Y. Wu, Y. Li, J. Li, K. He, Y. Xu, J. Zhang, and Y. Wang, Robust axion insulator and Chern insulator phases in a two-dimensional antiferromagnetic topological insulator, Nat. Mater. **19**, 522 (2020).

[23] J. Ge, Y. Liu, J. Li, H. Li, T. Luo, Y. Wu, Y. Xu, and J. Wang, High-Chern-number and high-temperature quantum Hall effect without Landau levels, Natl. Sci. Rev. **7**, 1280 (2020).

[24] G. van Miert, C. M. Smith, and V. Juričić, High-Chern-number bands and tunable Dirac cones in $\beta$-graphyne, Phys. Rev. B **90**, 081406(R) (2014).

[25] T. Cai, X. Li, F. Wang, S. Ju, J. Feng, and C.-D. Gong, Single-spin Dirac fermion and Chern insulator based on simple oxides, Nano Lett. **15**, 6434 (2015).

[26] Y.-J. Song, K.-H. Ahn, W. E. Pickett, and K.-W. Lee, Tuning ferromagnetic $BaFe_2(PO_4)_2$ through a high Chern number topological phase, Phys. Rev. B **94**, 125134 (2016).

[27] X. Kong, L. Li, O. Leenaerts, W. Wang, X.-J. Liu, and F. M. Peeters, Quantum anomalous Hall effect in a stable 1t-$YN_2$ monolayer with a large nontrivial band gap and a high Chern number, Nanoscale **10**, 8153 (2018).

[28] K. Ohgushi, S. Murakami, and N. Nagaosa, Spin anisotropy and quantum Hall effect in the kagome lattice: Chiral spin state based on a ferromagnet, Phys. Rev. B **62**, R6065(R) (2000).

[29] Z.-Y. Zhang, The quantum anomalous Hall effect in kagome lattices, J. Phys.: Condens. Matter **23**, 365801 (2011).

[30] G. Xu, B. Lian, and S.-C. Zhang, Intrinsic Quantum Anomalous Hall Effect in the Kagome Lattice $Cs_2LiMn_3F_{12}$, Phys. Rev. Lett. **115**, 186802 (2015).

[31] J.-X. Yin, S. S. Zhang, G. Chang, Q. Wang, S. S. Tsirkin, Z. Guguchia, B. Lian, H. Zhou, K. Jiang, I. Belopolski, N. Shumiya, D. Multer, M. Litskevich, T. A. Cochran, H. Lin, Z. Wang, T. Neupert, S. Jia, H. Lei, and M. Z. Hasan, Negative flat band magnetism in a spin-orbit-coupled correlated kagome magnet, Nat. Phys. **15**, 443 (2019).

[32] J.-X. Yin, W. Ma, T. A. Cochran, X. Xu, S. S. Zhang, H.-J. Tien, N. Shumiya, G. Cheng, K. Jiang, B. Lian, Z. Song, G. Chang, I. Belopolski, D. Multer, M. Litskevich, Z.-J. Cheng, X. P. Yang, B. Swidler, H. Zhou, H. Lin, T. Neupert, Z. Wang *et al.*, Quantum-limit Chern topological magnetism in $TbMn_6Sn_6$, Nature (London) **583**, 533 (2020).

[33] E. Liu, Y. Sun, N. Kumar, L. Muechler, A. Sun, L. Jiao, S.-Y. Yang, D. Liu, A. Liang, Q. Xu, J. Kroder, V. Süß, H. Borrmann, C. Shekhar, Z. Wang, C. Xi, W. Wang, W. Schnelle, S. Wirth, Y. Chen *et al.*, Giant anomalous Hall effect in a ferromagnetic kagome-lattice semimetal, Nat. Phys. **14**, 1125 (2018).

[34] L. Muechler, E. Liu, J. Gayles, Q. Xu, C. Felser, and Y. Sun, Emerging chiral edge states from the confinement of a magnetic Weyl semimetal in $Co_3Sn_3S_2$, Phys. Rev. B **101**, 115106 (2020).

[35] Q. Xu, E. Liu, W. Shi, L. Muechler, J. Gayles, C. Felser, and Y. Sun, Topological surface Fermi arcs in the magnetic Weyl semimetal $Co_3Sn_2S_2$, Phys. Rev. B **97**, 235416 (2018).

[36] Y. Sakai, Y. Kamihara, and M. Matoba, Magnetic properties of shandite-type $Co_3Sn_2S_{2-x}Se_x$, Phys. Status Solidi C **10**, 1130 (2013).

[37] P. E. Blochl, Projector augmented-wave method, Phys. Rev. B **50**, 17953 (1994).

[38] G. Kresse and J. Hafner, *Ab initio* molecular dynamics for liquid metals, Phys. Rev. B **47**, 558 (1993).

[39] G. Kresse and J. Furthmüller, Efficient iterative schemes for *ab initio* total-energy calculations using a plane-wave basis set, Phys. Rev. B **54**, 11169 (1996).

[40] J. P. Perdew, K. Burke, and M. Ernzerhof, Generalized Gradient Approximation Made Simple, Phys. Rev. Lett. **77**, 3865 (1996).

[41] H. J. Monkhorst and J. D. Pack, Special points for Brillouin-zone integrations, Phys. Rev. B **13**, 5188 (1976).

[42] A. Togo and I. Tanaka, First principles phonon calculations in materials science, Scr. Mater. **108**, 1 (2015).

[43] A. A. Mostofi, J. R. Yates, G. Pizzi, Y.-S. Lee, I. Souza, D. Vanderbilt, and N. Marzari, An updated version of WANNIER90: A tool for obtaining maximally-localised Wannier functions, Comput. Phys. Commun. **185**, 2309 (2014).

[44] X. Kong, L. Li, O. Leenaerts, X.-J. Liu, and F. M. Peeters, New group-V elemental bilayers: A tunable structure model with four-, six-, and eight-atom rings, Phys. Rev. B **96**, 035123 (2017).

[45] M. P. L. Sancho, J. M. L. Sancho, J. M. L. Sancho, and J. Rubio, Highly convergent schemes for the calculation of bulk and surface Green functions, J. Phys. F: Met. Phys. **15**, 851 (1985).

[46] Q. Wu, S. Zhang, H.-F. Song, M. Troyer, and A. A. Soluyanov, WannierTools: An open-source software package for novel topological materials, Comput. Phys. Commun. **224**, 405 (2018).

[47] See Supplemental Material at http://link.aps.org/supplemental/10.1103/PhysRevB.103.014410 for details.

[48] A. Jain, S. P. Ong, G. Hautier, W. Chen, W. D. Richards, S. Dacek, S. Cholia, D. Gunter, D. Skinner, G. Ceder, and K. A. Persson, Commentary: The materials project: A materials genome approach to accelerating materials innovation, APL Mater. **1**, 011002 (2013).

[49] K. Buschow, P. van Engen, and R. Jongebreur, Magneto-optical properties of metallic ferromagnetic materials, J. Magn. Magn. Mater. **38**, 1 (1983).

[50] T. Liu, W. Li, and G. Su, Spin-ordered ground state and thermodynamic behaviors of the spin-3/2 kagome Heisenberg antiferromagnet, Phys. Rev. E **94**, 032114 (2016).

[51] U. Wolff, Collective Monte Carlo Updating for Spin Systems, Phys. Rev. Lett. **62**, 361 (1989).

[52] F. J. Kahn, P. S. Pershan, and J. P. Remeika, Ultraviolet magneto-optical properties of single-crystal orthoferrites, garnets, and other ferric oxide compounds, Phys. Rev. **186**, 891 (1969).

[53] G. Y. Guo and H. Ebert, Band-theoretical investigation of the magneto-optical Kerr effect in Fe and Co multilayers, Phys. Rev. B **51**, 12633 (1995).

[54] H. Ebert, Magneto-optical effects in transition metal systems, Rep. Prog. Phys. **59**, 1665 (1996).

[55] Z. Q. Qiu and S. D. Bader, Surface magneto-optic Kerr effect, Rev. Sci. Instrum. **71**, 1243 (2000).

[56] J.-Y. You, Z. Zhang, X.-J. Dong, B. Gu, and G. Su, Two-dimensional magnetic semiconductors with room Curie temperatures, Phys. Rev. Res. **2**, 013002 (2020).